Hybrid mode calculations for novel photonic crystal fibers

Waleed S. Mohammed

Laurent Vaissié

Eric G. Johnson
University of Central Florida

Hybrid mode calculations for novel photonic crystal fibers

Waleed S. Mohammed
Laurent Vaissié, MEMBER SPIE
Eric G. Johnson
University of Central Florida
Center for Research and Education in Optics and Lasers
School of Optics
Orlando, Florida 32816-2700

Abstract. Photonic crystal fibers (PCFs) are quite useful for confining and guiding light with interesting modal properties. The scattering matrix method is used to calculate the higher order modes guided in a PCF. The model is derived from the solution of the boundary condition problem taking into consideration the coupling between the electric and the magnetic fields. Results are presented for novel fibers that allow for only azimuthal modes.
[DOI: 10.1117/1.1589758]

Subject terms: photonic crystal fibers; hybrid modes; vortex element; scattering matrix method.

Paper 020457 received Oct. 17, 2002; revised manuscript received Jan. 28, 2003; accepted for publication Feb. 13, 2003.

1 Introduction

A photonic crystal fiber (PCF) is a cylindrical structure composed of a 2-D lattice of air holes in a homogeneous dielectric medium.[1] Defects in this lattice are responsible for creating localized regions where modes of light can exist and other regions where light cannot; thereby, tailoring both the modal structure and dispersion characteristics of the PCF without having to resort to complex refractive index profiles in the fiber.[2] This guiding, or modal confinement, of the light is governed by two fundamental mechanisms.[3] The first is based on an effective refractive index that is created by varying the lattice density as a function of position[4] across the PCF. The second mechanism utilizes the concepts of photonic bandgap (PBG) engineering to confine the light in the desired modes. Given these two mechanisms of guiding light in a PCF, modeling the modal structure of these devices requires that both effective index and PBG concepts be represented as appropriate.[5]

In this paper, we apply the scattering matrix method, presented in Refs. 6 and 7, to the PCF to model the hybrid modes of a guiding structure. As a continuation of the work done by Centeno and Felbacq in Ref. 7, we extend this approach to an eigenvalue problem for estimating the propagating modes of an arbitrarily shaped cavity composed of a holey fiber. Moreover, we include the chromatic dispersion of fused silica material using the Sellmeier coefficients. As a result of implementing the scattering matrix method, nontraditional designs of photonic crystal cavities are addressed for the first time. As a result, a unique PCF design is introduced that allows for only higher order azimuthal modes in a preferred rotational direction.

2 Theoretical Approach

Figure 1 shows the geometry of the problem. Each dielectric rod, of index j, is defined by its location vector $\mathbf{r}_j$ measured from a reference point $\mathbf{O}$, a refractive index n_j, and a radius R_j. To solve the problem of light propagating through the inhomogeneous PCF, we solve the homogeneous problem in each medium (inside and outside the rods) taking into account the effect of the structure. The scattered light from each rod is calculated from Maxwell's equations with the appropriate application of the boundary conditions at that rod. The main goal is to simplify the inhomogeneous wave equation to an eigenvalue problem. The solution of this eigenvalue problem represents the allowed, or guided, modes. We calculate the complex propagation constants of these modes using the false position method. The imaginary part indicates how leaky the mode is. The scattered field distributions can be calculated from the eigenvectors. The total scattered field at all points in space is the superposition of the field scattered from each individual rod.

The allowed modes of the electric and magnetic fields are represented in cylindrical coordinates with[6]

$$\overline{\mathbf{F}}(r,\phi,z)=\overline{\mathbf{F}}(r,\phi)\exp[i(\varpi t-\beta z)], \tag{1}$$

where $\overline{\mathbf{F}}$ represents the z components of both the electric and magnetic fields

$$\overline{\mathbf{F}}=\begin{pmatrix} E_z \\ H_z \end{pmatrix}.$$

The propagation constant β corresponds to the z component of the wave vector according to the coordinates shown in Fig. 2. The figure shows three field components around rod j: the scattered light; the local incident light, defined as the summation of light scattered from all other rods; and the transmitted light. The fields are represented by their respective Fourier-Hankel expansions[6] in Eqs. (2)–(4):

$$\overline{\mathbf{F}}^s(r,\phi)=\sum_{j=1}^{N_{\text{rods}}}\sum_{m=-N}^{N}\overline{\mathbf{b}}_m H_m^{(2)}(\chi_1 r_j)\exp(im\phi_j),$$

$$\overline{\mathbf{b}}_m=\begin{pmatrix} b_m^e \\ b_m^h \end{pmatrix}, \tag{2}$$

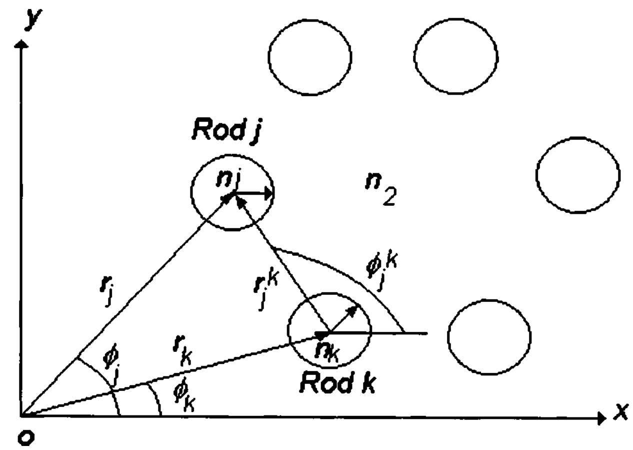

Fig. 1 PCF consists of a periodical air pattern with a deformation produced by removing the central air rod. The z axis represents the direction of propagation, d is the lattice constant (the separation between the rods), and R is the radius of each rod.

$$\overline{\mathbf{F}}_j^{\text{loc}}(r,\phi)=\sum_{m=-N}^{N}\overline{\mathbf{a}}_m J_m(\chi_1 r_j)\exp(im\phi_j),\quad \overline{\mathbf{a}}_m=\begin{pmatrix}a_m^e\\a_m^h\end{pmatrix}, \tag{3}$$

$$\overline{\mathbf{F}}_j^{t}(r,\phi)=\sum_{m=-N}^{N}\overline{\mathbf{c}}_m J_m(\chi_2 r_j)\exp(im\phi_j),\quad \overline{\mathbf{c}}_m=\begin{pmatrix}c_m^e\\c_m^h\end{pmatrix}. \tag{4}$$

The superscripts e and h represent the electric and magnetic fields, respectively; ϕ_j and r_j are the angle and distances measured from the reference point **O** to the center of rod j; and χ_1 and χ_2 are the tangential components of the wave vector outside and inside the air rod, respectively. They are related to β through the dispersion relations

$$\chi_i=(k_o^2 n_i^2-\beta^2)^{1/2}\quad i=1,2. \tag{5}$$

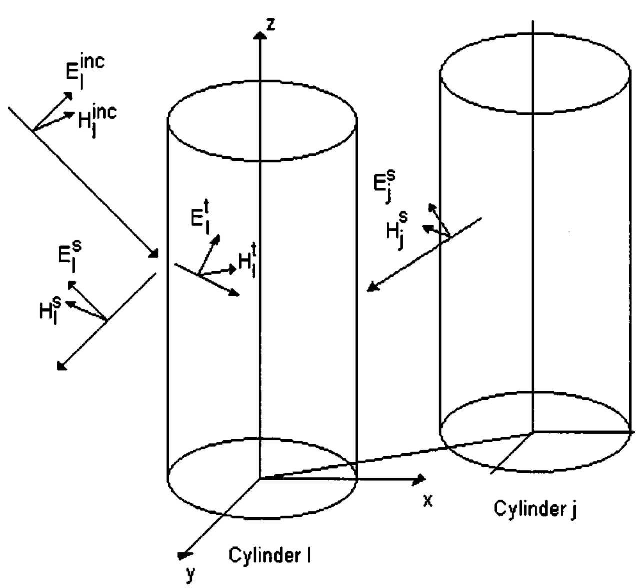

Fig. 2 Cylindrical coordinates originated at the center of one air rod: F^s, F^{loc}, and F^t represent the scattered, local incident, and transmitted electric/magnetic fields at an air rod interface.

However, we must apply the boundary conditions to each rod. The appendix shows the solution of the boundary condition problem. From the Eqs. (15) and (16), we get a linear relation between $\overline{\mathbf{a}}$ and $\overline{\mathbf{b}}$

$$\overline{\mathbf{b}}=\overline{\overline{\mathbf{S}}}\cdot\overline{\mathbf{a}}, \tag{6}$$

where $\overline{\overline{\mathbf{S}}}$ is a square matrix of dimensions $(2N+1)N_{\text{rods}}\times(2N+1)N_{\text{rods}}$, which represents the scattering matrix of the photonic crystal structure. This matrix relates the scattered field to the local incident one on each air rod. The geometry of the structure is implicitly included in the matrix $\overline{\overline{\mathbf{S}}}$ as the fields in Eqs. (2)–(4) are expanded around the centers of each air rod. The total scattered field in Eq. (2) is calculated as the interference between the fields scattered from each rod.

Although the information regarding the geometry of the structure is hidden in $\overline{\overline{\mathbf{S}}}$, we still need to calculate the crosstalk between the rods. Recalling that the locally incident field on rod j is defined as the summation of the light scattered from all the rods except j, which is set to zero to solve for the allowed propagating modes, we are enabled to express the following formula for the local field:

$$E_j^{\text{loc}}=\sum_{k\neq j}E_k^s,$$
$$\sum_m^M a_m^e J_m(\chi_1 r_j)\exp(iq\phi_j)$$
$$=\sum_{k\neq j}\sum_q^M b_q^e H_q^{(2)}(\chi_1 r_k)\exp(iq\phi_j). \tag{7}$$

Applying the expansion of $H_q^{(2)}(\chi_1 r_k)\exp(iq\phi_j)$ around r_j, as presented in Ref. 6, to Eq. (7) we get the following relation between the local incident and the scattered field coefficients:

$$\overline{\mathbf{a}}_m=\sum_{k\neq j}\sum_q^M\overline{\mathbf{b}}_m T_{m,q,j,k},$$

$$T_{m,q,j,k}=\exp[i(q-m)\phi_{kl}^{jk}]H_{m-q}^{(2)}(\chi_1 r_k^j), \tag{8}$$

which can be written in the vector form

$$\overline{\mathbf{a}}=\overline{\overline{\mathbf{T}}}\cdot\overline{\mathbf{b}}. \tag{9}$$

In Eq. (9), $\overline{\overline{\mathbf{T}}}$ represents the crosstalk between the rods. Recalling the linear relation between $\overline{\mathbf{a}}$ and $\mathbf{b}$ in Eq. (6), we can write Eq. (9) as

$$(\overline{\overline{\mathbf{I}}}-\overline{\overline{\mathbf{S}}}\cdot\overline{\overline{\mathbf{T}}})\cdot\overline{\mathbf{b}}=0\quad\text{or}\quad\overline{\overline{\mathbf{M}}}(\beta)\cdot\overline{\mathbf{b}}=0. \tag{10}$$

Equation (10) represents an eigenvalue problem for which the eigenvalue is zero. The solutions correspond to the eigenmodes of the resulting PCF.

3 Numerical Results

In this section, results are presented for various PCF structures. In the first design, we present the modal dispersion curves for a multimode PCF taking into account the material dispersion of the fused silica material using the Sellmeier coefficients. In the second part we present a circular cavity with a cladding formed of air holes located on spiral trajectories, what we call a vortex PCF. This arrangement of the air holes leads to a preferential direction of rotation of the higher order modes. In all of the cases presented here, only nine circular harmonic functions were required, since we do not get significant precision improvement[8] for increasing *N*.

As a first step, we compared the dispersion calculations for a single-mode PCF to the results obtained using the full vector modal technique demonstrated by Ferrando.[5] The average mean square error in the effective mode index calculated using the scattering matrix method (SMM) compared to the one used by Ferrando was about 4.823 $\times 10^{-4}$. This shows a very good agreement between the two methods. The material dispersion is not included in this part.

3.1 *Results for Multimode Holey Fiber*

In this part, we study the dispersion properties of two multimode photonic crystal fibers; a step-index PCF and a ring-core PCF. The step-index PCF has an approximate core radius of 4.41 μm. The cladding region consists of a lattice of air holes with a 0.295-μm radius and 3.5-μm holes spacing *D*, as shown in Fig. 3(a). The same figure shows the refractive index profile across the fiber. The cladding index is the effective refractive index of the lattice calculated as shown in

$$n_{\mathrm{eff}}(\lambda)=\frac{(\mathrm{area}_{\mathrm{SiO}_2}\times n_{\mathrm{SiO}_2}(\lambda)+\mathrm{area}_{\mathrm{holes}}\times 1)}{\mathrm{area}_{\mathrm{cell}}}. \quad (11)$$

This does not contradict the fact that the light is confined because of the PBG effect. Figure 3(b) shows the dispersion curves for the fundamental mode and two higher order modes. The material dispersion is included through the use of Sellmeier coefficients for fused silica material (Ref. 9, p. 80). As shown in Fig. 3(b), for normalized frequencies less than 2 the PCF works as a single-mode fiber. Increasing the frequency, thus decreasing the wavelength, will enable the higher order modes to be guided modes. Hence, the multimode dispersion will be effective in this case. For traditional fibers, changing the material properties can change dispersion properties of the fiber. In PCF, changing the air holes size will alter the modal properties hence the multimode dispersion

In the second example, we studied the dispersion and field distribution of a multimode ring core PCF. The structure together with the refractive index profile is shown in Fig. 4(a). The dispersion curves for the fundamental mode and the first four higher order modes are shown in Fig. 4(b). Notice that more modes will exist for normalized frequencies larger than 1.7 but we did not include them in this graph. Figures 5 and 6 show the electric field distributions for the fundamental and the first two higher order modes. The fundamental mode has a minimum intensity at the central part. Besides, the higher order modes consist of two degenerate skew modes rotating in opposite directions. In

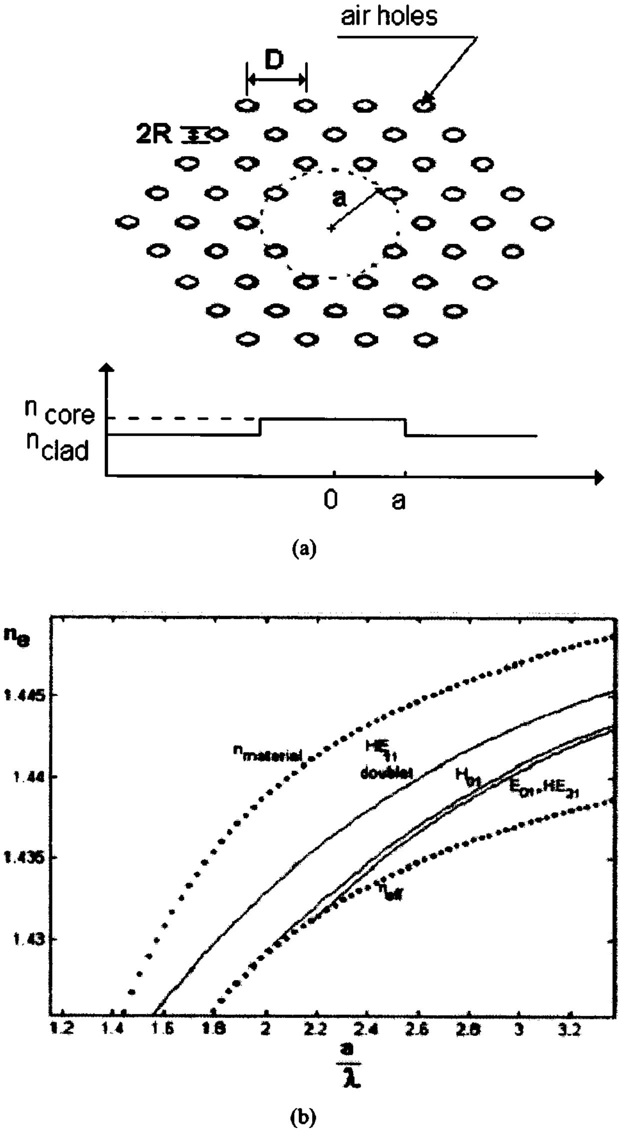

Fig. 3 (a) Multimode PCF structure formed by removing the four central rods forming a core of diameter 8.82 μm. The cladding refractive index n_{clad} is the average refractive index calculated by integration over one cell area. (b) The dispersion curves for the fundamental and higher order modes.

the next part, we show an asymmetrical PCF design that allows only one preferential direction of rotation of the higher order modes.

3.2 *Vortex Photonic Crystal Fiber*

In this part, we aim to design a cavity with a preferable direction of rotation of the Poynting vector while propagating through the PCF. In cylindrical symmetric waveguides such as fibers and, to some extent, a traditional PCF, higher order degenerate modes rotate in opposite directions. To have a preferential direction of propagation, we should not be restricted to the symmetry or the periodicity of the lattice. We call such structures asymmetrical PCFs.

Figure 7 shows a nontraditional photonic crystal structure with air holes allocated on spiral form. In this design, each set of 16 holes is located on a circle of larger radius than the previous set such that $r_{n+1}-r_n=2.8\ \mu$m. Each set

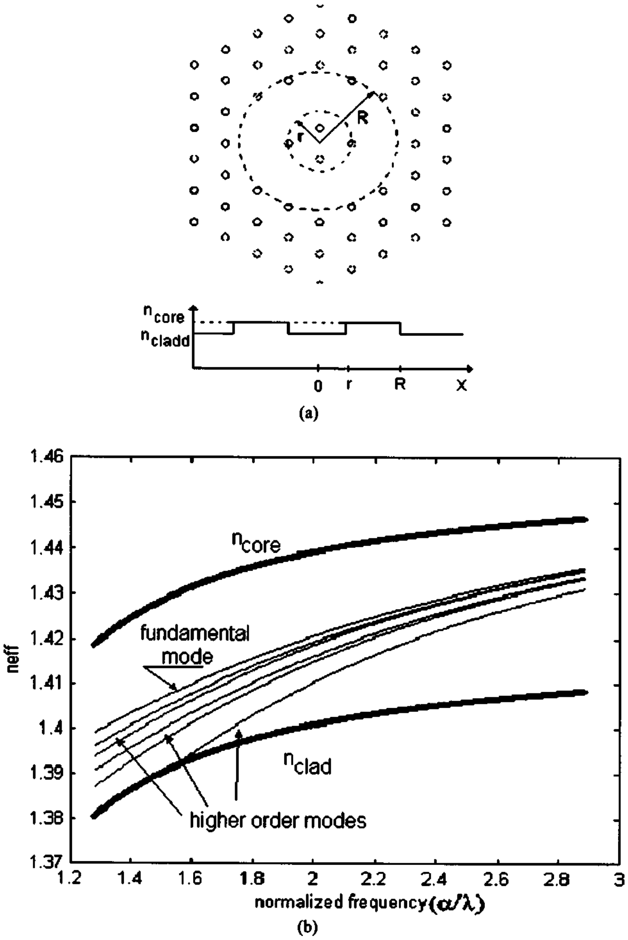

Fig. 4 (a) Multimode ring core PCF structure and (b) dispersion curves for the fundamental and four higher order modes.

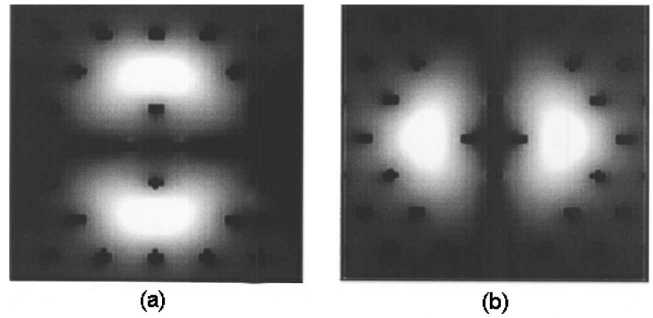

Fig. 6 First higher order mode for the multimode ring core PCF.

of air holes is rotated by an angle of 11.25 deg relative to the previous set. The radius of the core is set to be 6.3 μm. The first higher order mode presents at $n_{\mathrm{eff}}=1.450685-i\times 7.3067\times 10^{-5}$. The electric field components distributions of the first higher order mode is shown in Figs. 8(a) and 9(a). Figures 8(b) and 9(b) show the phases of E_x and E_y of the first degenerate mode. Observing the phase distributions, we can, approximately, write the two field components within the core as

$$E_x=|E_x(x,y)|e^{-i\theta} \quad \text{and}$$

$$E_y=|E_y(x,y)|\exp[-i(\theta+\pi/2)]. \tag{12}$$

Equation (12) represents a right-handed circularly polarized electric field, because of the $\pi/2$ phase shift between the electric field components, with a phase ramp. Figure 10 shows the transverse component of the Poynting vector in the core region that shows a clockwise rotation of the beam in the transversal plane. This leads to a skew motion of the light while propagating through the fiber. The second higher order modes, at $n_{\mathrm{eff}}=1.448679-i\times 0.0011$, has amplitude and phase distributions for both fields components, as shown in Fig. 11. From the value of the imaginary part of n_{eff} and the amplitude distribution of the field components one can conclude that this mode is a leaky cladding mode. In spite of being a leaky mode, the phase distribution is similar to that of a vortex lens with transmittance of $\exp(-i2\theta)$. Thus, if we design a fiber with larger core, which enables more guided modes with better confinement, then the m'th higher order mode will have an approximated

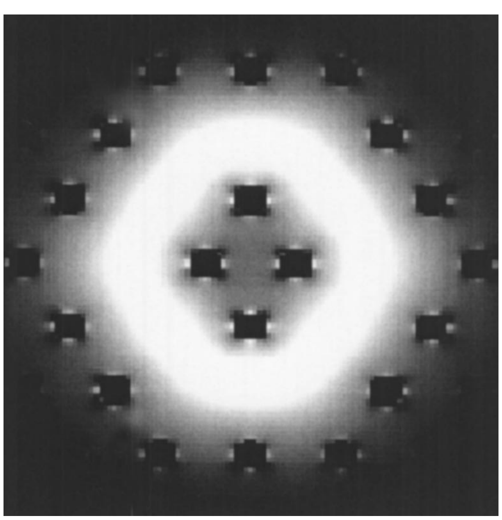

Fig. 5 Field components distribution of the fundamental mode for the multimode ring core PCF.

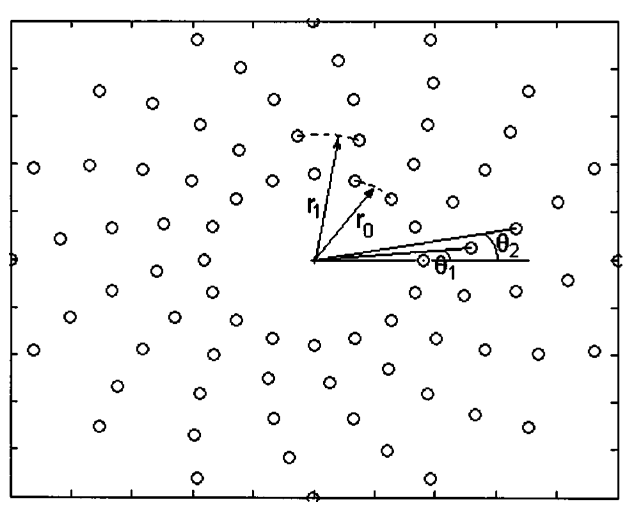

Fig. 7 Geometry of the spiral cladding PCF.

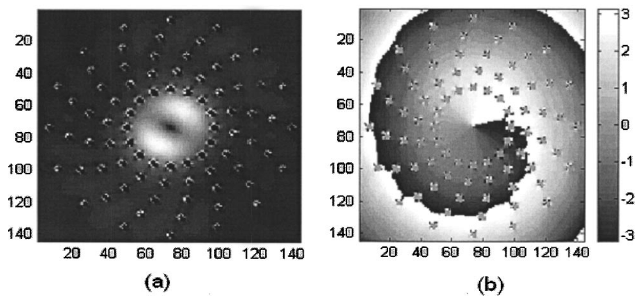

Fig. 8 Amplitude distribution of (a) E_x and phase distributions of (b) E_x of the first-order mode.

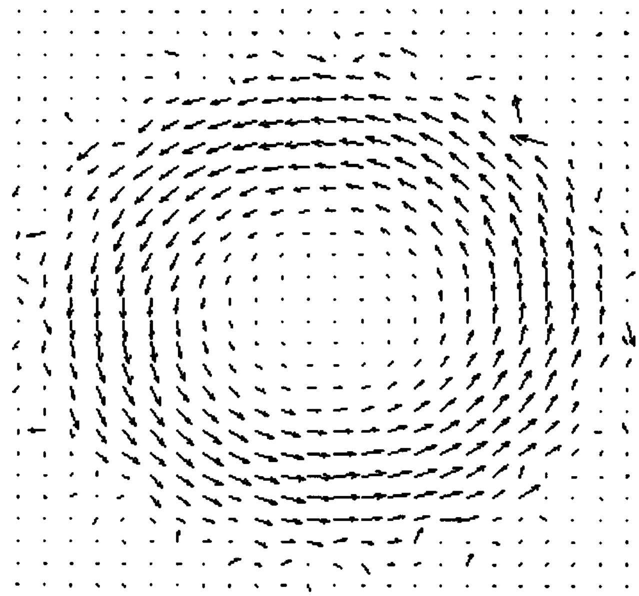

Fig. 10 Direction of the transversal Poynting vector within the core.

phase distribution of $m\theta$. Although these higher order modes have reasonably high loss terms in the refractive index (which makes them leaky), they illustrate the possibility of manipulating the spatial amplitude and phase distributions of the allowed higher order modes by rearranging the cladding air holes locations.

As mentioned in this section, the high-order modes suffer from high losses. This requires designs that improve confinement of the light in the central region. As an example, a photonic crystal cladding of periodical air holes can be added around the vortex PCF. The main disadvantage of this design is the addition of extra modes because of the change of the geometry of the structure. Increasing the size of the air holes will improve the confinement in the first higher order modes but, on the other hand, that will increase the number of guided modes.

Although the proposed vortex PCF has high losses, small portions of this fiber can be used to excite higher order modes when spliced with multimode fiber or as a source for particle trapping applications.

4 Conclusion

The SMM was used successfully to calculate the modal properties of PCFs of different core shapes and nontraditional arrangements of the air hole lattice. A complete field solution was obtained over the working space for the different guided modes inside the fiber with no restrictions over the refractive index contrast or the periodicity or symmetry of the structure. We presented modal solutions and dispersion curves for multimode step-index and ring-core PCF's. The method was used successfully to calculate the effect of changing the geometry of the structure over the dispersion properties of the PCF. Also, we introduced a circular cavity with spiral cladding, which we call a vortex PCF. A complete vector solution of this design showed the presence of higher order modes that rotate in a preferable direction, similar to the skew rays of a multimode fiber. The main disadvantage of this design is that the higher order modes are leaky. Thus, we must come up with designs that have better confinement. These unique properties of the higher order modes open a new field of applications of the PCFs. Using the SMM to model the hybrid modes in a PCF has advantages from calculation and design points of view as each rod is represented by its location and radius. As a continuation of this work, different designs can be proposed to improve the confinement of the skew modes. We may also need to study the dispersion properties of the multicore PCF in compared to the regular multicore fibers.

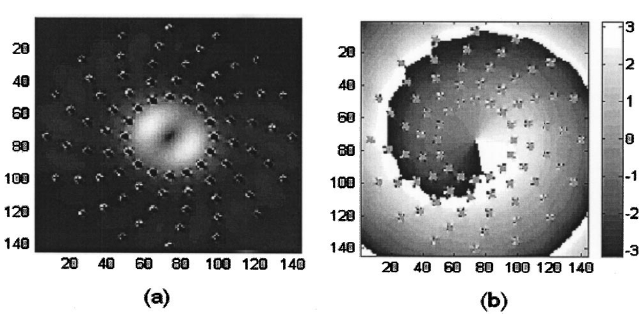

Fig. 9 Amplitude distribution of (a) E_y and phase distributions of (b) E_y of the first-order mode.

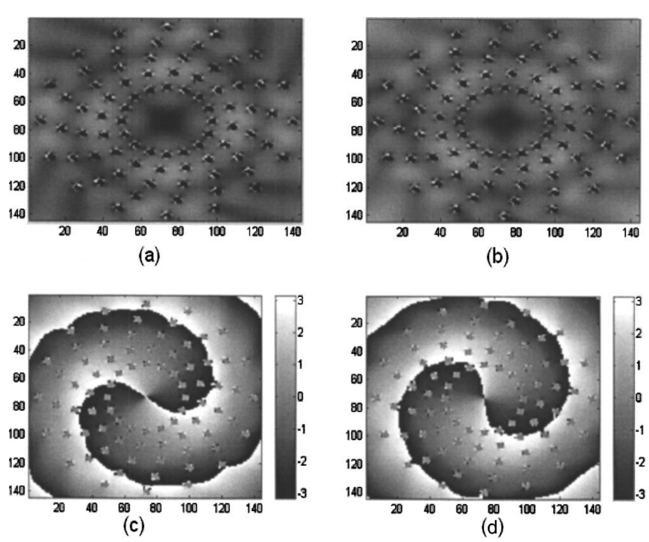

Fig. 11 Amplitude distribution of (a) E_x and (b) E_y and phase distributions of (c) E_x and (d) E_y for the second higher mode.

Also, this method can be used to simulate pulse propagation through any PCF structure. One can also optimize the dispersion properties of the structure by changing its geometry.

5 Appendix: Solving the Boundary Condition Problem

To calculate the scattered fields in Eq. (2), we must first apply the boundary conditions at the air-dielectric interface at each rod, $r=R$, as shown in Fig. 2. Applying the continuity of the z components of the fields we get the following equations, using the field expansions in Eqs. (2)–(4) we get the following vector equation:

$$\begin{pmatrix} \frac{J_m(\chi_1 R)}{J_m(\chi_2 R)} & 0 \\ 0 & \frac{J_m(\chi_1 R)}{J_m(\chi_2 R)} \end{pmatrix} \cdot \overline{\mathbf{a}}_m + \begin{pmatrix} \frac{H_m^{(2)}(\chi_1 R)}{J_m(\chi_2 R)} & 0 \\ 0 & \frac{H_m^{(2)}(\chi_1 R)}{J_m(\chi_2 R)} \end{pmatrix} \cdot \overline{\mathbf{b}}_m = \overline{\mathbf{c}}_m . \quad (13)$$

From the continuity of the ϕ components of the electric and magnetic fields, expressed as a function of the z components of the fields, we get the following equations:

$$\begin{pmatrix} \frac{\omega\epsilon_1}{\chi_1 J_m'(\chi_1 R)} & \frac{i\beta m}{R\chi_1^2} J_m(\chi_1 R) \\ \frac{i\beta m}{R\chi_1^2} J_m(\chi_1 R) & \frac{\omega\mu}{\chi_1} J_m'(\chi_1 R) \end{pmatrix} \cdot \overline{\mathbf{a}}_m + \begin{pmatrix} \frac{\omega\epsilon_1}{\chi_1} H_m^{(2)\prime}(\chi_1 R) & \frac{i\beta m}{R\chi_1^2} H_m^{(2)}(\chi_1 R) \\ \frac{i\beta m}{R\chi_1^2} H_m^{(2)}(\chi_1 R) & \frac{\omega\mu}{\chi_1} H_m^{(2)\prime}(\chi_1 R) \end{pmatrix} \cdot \overline{\mathbf{b}}_m = \begin{pmatrix} \frac{\omega\epsilon_2}{\chi_2} J_m'(\chi_2 R) & \frac{i\beta m}{R\chi_2^2} J_m(\chi_2 R) \\ \frac{i\beta m}{R\chi_2^2} J_m(\chi_2 R) & \frac{\omega\mu}{\chi_2} J_m'(\chi_2 R) \end{pmatrix} \cdot \overline{\mathbf{c}}_m . \quad (14)$$

We can combine Eqs. (14) and (15) in a matrix form taking into account all the expansion coefficients, seven coefficients in our case, to get the following vector equation:

$$\bar{\bar{\mathbf{A}}}_1 \cdot \overline{\mathbf{a}} + \bar{\bar{\mathbf{B}}}_1 \cdot \overline{\mathbf{b}} = \overline{\mathbf{c}}, \quad (15)$$

$$\bar{\bar{\mathbf{A}}}_2 \cdot \overline{\mathbf{a}} + \bar{\bar{\mathbf{B}}}_2 \cdot \overline{\mathbf{b}} = \bar{\bar{\mathbf{C}}}_2 \cdot \overline{\mathbf{c}}, \quad (16)$$

where

$$\overline{\mathbf{a}} = \begin{pmatrix} a_1^e \\ \vdots \\ a_M^e \\ a_1^h \\ \vdots \\ a_M^h \end{pmatrix}, \quad \overline{\mathbf{b}} = \begin{pmatrix} b_1^e \\ \vdots \\ b_M^e \\ b_1^h \\ \vdots \\ b_M^h \end{pmatrix}, \quad \overline{\mathbf{c}} = \begin{pmatrix} c_1^e \\ \vdots \\ c_M^e \\ c_1^h \\ \vdots \\ c_M^h \end{pmatrix},$$

and $\bar{\bar{\mathbf{A}}}_1$, $\bar{\bar{\mathbf{B}}}_1$, $\bar{\bar{\mathbf{A}}}_2$, $\bar{\bar{\mathbf{B}}}_2$, and $\bar{\bar{\mathbf{C}}}_2$ are square matrices as defined next, and M is the number of expansion coefficients.

$$\bar{\bar{\mathbf{A}}}_1 = \begin{pmatrix} \frac{\bar{\bar{\mathbf{J}}}(\chi_1 R)}{\bar{\bar{\mathbf{J}}}(\chi_2 R)} & 0 \\ 0 & \frac{\bar{\bar{\mathbf{J}}}(\chi_1 R)}{\bar{\bar{\mathbf{J}}}(\chi_2 R)} \end{pmatrix}, \quad \bar{\bar{\mathbf{B}}}_1 = \begin{pmatrix} \frac{\bar{\bar{\mathbf{H}}}^{(2)}(\chi_1 R)}{\bar{\bar{\mathbf{J}}}(\chi_2 R)} & 0 \\ 0 & \frac{\bar{\bar{\mathbf{H}}}^{(2)}(\chi_1 R)}{\bar{\bar{\mathbf{J}}}(\chi_2 R)} \end{pmatrix}, \quad (17)$$

$$\bar{\bar{\mathbf{A}}}_2 = \begin{pmatrix} \frac{\omega\epsilon_1}{\chi_1} \bar{\bar{\mathbf{J}}}'(\chi_1 R) & \frac{i\beta m}{R\chi_1^2} \bar{\bar{\mathbf{J}}}(\chi_1 R) \\ \frac{i\beta m}{R\chi_1^2} \bar{\bar{\mathbf{J}}}(\chi_1 R) & \frac{\omega\mu}{\chi_1} \bar{\bar{\mathbf{J}}}'(\chi_1 R) \end{pmatrix}, \quad \bar{\bar{\mathbf{B}}}_2 = \begin{pmatrix} \frac{\omega\epsilon_1}{\chi_1} \bar{\bar{\mathbf{H}}}^{(2)\prime}(\chi_1 R) & \frac{i\beta m}{R\chi_1^2} \bar{\bar{\mathbf{H}}}^{(2)}(\chi_1 R) \\ \frac{i\beta m}{R\chi_1^2} \bar{\bar{\mathbf{H}}}^{(2)}(\chi_1 R) & \frac{\omega\mu}{\chi_1} \bar{\bar{\mathbf{H}}}^{(2)\prime}(\chi_1 R) \end{pmatrix}, \quad (18)$$

$$\bar{\bar{\mathbf{C}}}_2 = \begin{pmatrix} \frac{\omega\epsilon_2}{\chi_2} \bar{\bar{\mathbf{J}}}'(\chi_2 R) & \frac{i\beta m}{R\chi_2^2} \bar{\bar{\mathbf{J}}}(\chi_2 R) \\ \frac{i\beta m}{R\chi_2^2} \bar{\bar{\mathbf{J}}}(\chi_2 R) & \frac{\omega\mu}{\chi_2} \bar{\bar{\mathbf{J}}}'(\chi_2 R) \end{pmatrix},$$

$$\bar{\bar{\mathbf{J}}} = \begin{pmatrix} J_{-(M/2)} & \cdots & 0 \\ \vdots & \cdots & \vdots \\ 0 & \cdots & J_{M/2} \end{pmatrix}, \quad \text{and}$$

$$\bar{\bar{\mathbf{H}}}^{(2)} = \begin{pmatrix} H_{-(M/2)}^{(2)} & \cdots & 0 \\ \vdots & \cdots & \vdots \\ 0 & \cdots & H_{M/2}^{(2)} \end{pmatrix}. \quad (19)$$

References

1. R. Ghosh et al., ''Modal characteristics of few-mode silica-based photonic crystal fibers,'' *Opt. Quantum Electron.* **32**, 963–970 (2000).
2. M. Qiu, ''Analysis of guided modes in photonic crystal fibers using

the finite-difference time-domain method,'' *Microwave Opt. Technol. Lett.* **30**(5), (2001).
3. T. M. Monro, ''Holey optical fibers: an effective modal method,'' *J. Lightwave Technol.* **11**, 1093–1102 (1999).
4. T. A. Birks, ''Endlessly single-mode photonic crystal fiber,'' *Opt. Lett.* **22**, 961–963 (1997).
5. A. Ferrando, ''Vector description of higher-order modes in photonic crystal fibers,'' *J. Opt. Soc. Am. A* **17**, 1333–1336 (2000).
6. J. Yonekura, M. Ikeda, and T. Baba, ''Analysis of finite 2-D photonic crystals of columns and light wave devices using the scattering matrix method,'' *J. Lightwave Technol.* **17**(8), 1500–1508 (1999).
7. E. Centeno and D. Felbaq, ''Rigorous vector diffraction of electromagnetic waves by bidimensional photonic crystals,'' *J. Opt. Soc. Am. A* **17**(2), 320–327 (2000).
8. D. Felbacq, G. Tayeb, and D. Maystre, ''Scattering by a random set of parallel cylinders,'' *J. Opt. Soc. Am. A* **11**(9), 2526 (1994).
9. K. Okamoto, *Fundamentals of Optical Waveguides*, Academic (1992).

Waleed S. Mohammed received his BSc degree in electronics and electrical communications engineering in 1996 and his MSc degree in computer engineering in 1999, both from Cairo University, Egypt, and his MSc degree in optics in 2001 from the School of Optics/CREOL, Orlando, Florida, where he is currently working toward his PhD degree in the field of micro- and nanophotonics.

Laurent Vaissié received his MSc degree in engineering physics from Ecole Naionale Supérieure de Physique, Marseille, in 1998. He joined the School of Optics/CREOL in 1999 and received his MSc degree in optics in 2001. He is currently working toward his PhD degree in the field of integrated optics.

Eric G. Johnson received his BSc degree in physics from Purdue University in 1985, his MSc degree in electrical engineering from the University of Central Florida in 1989, and his PhD degree in electrical engineering from the University of Alabama, Huntsville, in 1996. Since 2000 he has been an assistant professor of optical engineering with the School of Optics/CREOL. Prior to joining CREOL, he was the vice president of research and development with Digital Optics Corporation in Charlotte, North Carolina. He has also held positions at SY Technology, Teledyne Brown Engineering, and Martin Marietta. His research interests include diffractive and microphotonic systems, data communications, and nanophotonics. He is a member of OSA and IEEE.